

HS-3D-NeRF: 3D Surface and Hyperspectral Reconstruction From Stationary Hyperspectral Images Using Multi-Channel NeRFs

KIBON KU*, TALUKDER Z. JUBERY*, ADARSH KRISHNAMURTHY†, and BASKAR GANAPATHYSUBRAMANIAN†, Iowa State University, USA

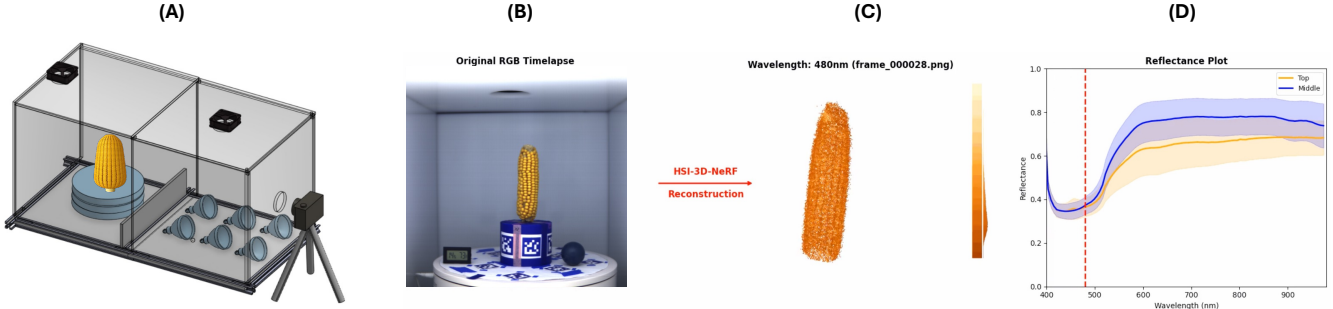


Fig. 1. Schematic of the stationary camera imaging system for hyperspectral NeRF-based point cloud reconstruction in high-throughput plant phenotyping. In this setup, each plant is conveyed to a rotating turntable marked against a Teflon (PTFE) background. Over a full rotation, a tripod-mounted stationary camera captures high-resolution images that serve as input for HS-3D-NeRF techniques to generate 3D reconstructions. This streamlined approach eliminates the need for complex moving-camera rigs, aligning with the objectives of efficient, scalable agricultural imaging. The right shows the different PCD reconstructions using HS-3D-NeRF and spectral signatures on the circled regions.

Advances in hyperspectral imaging (HSI) and 3D reconstruction have enabled accurate, high-throughput characterization of agricultural produce quality and plant phenotypes, both essential for advancing agricultural sustainability and breeding programs. HSI captures detailed biochemical features of produce, while 3D geometric data substantially improves morphological analysis. However, integrating these two modalities at scale remains challenging, as conventional approaches involve complex hardware setups incompatible with automated phenotyping systems. Recent advances in neural radiance fields (NeRF) offer computationally efficient 3D reconstruction but typically require moving-camera setups, limiting throughput and reproducibility in standard indoor agricultural environments. To address these challenges, we introduce HSI-SC-NeRF, a stationary-camera multi-channel NeRF framework for high-throughput hyperspectral 3D reconstruction targeting postharvest inspection of agricultural produce. Multi-view hyperspectral data is captured using a stationary camera while the object rotates within a custom-built Teflon imaging chamber providing diffuse, uniform illumination. Object poses are estimated via ArUco calibration markers and transformed to the camera frame of reference through simulated pose transformations, enabling standard NeRF training on stationary-camera data. A multi-channel NeRF formulation optimizes reconstruction across all hyperspectral bands jointly using a composite spectral loss, supported by a two-stage training protocol that decouples geometric initialization from radiometric refinement. Experiments on three agricultural produce samples demonstrate high spatial reconstruction accuracy and strong spectral fidelity across the visible and near-infrared spectrum, confirming the suitability of HSI-SC-NeRF for integration into automated agricultural workflows.

*Equal contribution

†Corresponding authors

Authors' Contact Information: Kibon Ku, kibona9@iastate.edu; Talukder Z. Jubery, znjubery@iastate.edu; Adarsh Krishnamurthy, adarsh@iastate.edu; Baskar Ganapathysubramanian, baskarg@iastate.edu, Iowa State University, Ames, Iowa, USA.

CCS Concepts: • **Applied computing** → **Agriculture**; • **Computing methodologies** → **Hyperspectral imaging**; *Computational photography*; Reflectance modeling.

Additional Key Words and Phrases: Hyperspectral Imaging, Multi-channel NeRFs, Hyperspectral 3D Reconstruction

1 Introduction

High-throughput and precise characterization of plant phenotypes and produce quality is critical for advancing food security, enhancing nutritional quality, and promoting agricultural sustainability [Gupta et al. 2024; Sarkar et al. 2023]. Advanced imaging techniques that integrate spatial and spectral information enable simultaneous morphological and biochemical trait analysis, accelerating breeding programs and improving supply chain monitoring. Hyperspectral imaging (HSI), which captures reflectance across hundreds of narrow spectral bands spanning the visible to near-infrared spectrum (400–1000 nm), has proven invaluable in agriculture due to its sensitivity to physiological indicators such as chlorophyll content, water stress, and biochemical composition [Song et al. 2024; Li et al. 2025].

Traditional HSI methods generally produce 2D hyperspectral data, limiting their ability to accurately characterize 3D plant architecture or produce morphology. As illustrated in Fig. 2, surface curvature and self-occlusion can cause a defect region to be visible from one viewing angle but partially or fully hidden from another, resulting in missed detections and biased severity estimates under single-view analysis. This limitation has motivated significant research into integrating hyperspectral data with 3D structural reconstruction using techniques such as Structure-from-Motion (SfM), Multi-View Stereo (MVS) [Eltner and Sofia 2020; Chen et al. 2019], or active depth sensing technologies such as LiDAR [Wang and Glennie 2015; Cai et al.

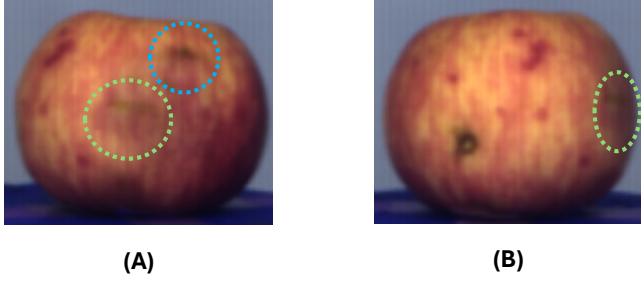


Fig. 2. Motivation for hyperspectral imaging (HSI) in 3D. Two views of the same apple show viewpoint-dependent bruise visibility: one ROI is visible in view (A) but occluded in view (B), motivating HSI with 3D reconstruction for more complete surface assessment.

2023]. However, these approaches often involve complex hardware setups with high operational costs and demanding calibration procedures, limiting their scalability in high-throughput agricultural workflows [Andújar et al. 2018; Tang et al. 2022; Paturkar et al. 2021; Lu 2023].

Recent advances in neural implicit representations, particularly neural radiance fields (NeRF), offer robust and scalable alternatives for 3D reconstruction [Mildenhall et al. 2021]. NeRFs model volumetric scenes by learning radiance and density distributions from multi-view images without explicit geometric constraints, and can replicate complex view-dependent effects such as translucency and occlusion that are common in agricultural subjects [Sarkar et al. 2023; Cuevas-Velasquez et al. 2020; Feng et al. 2023]. The integration of HSI into the NeRF framework further enables simultaneous recovery of geometry and spectral reflectance information at each spatial point [Chen et al. 2024].

Despite these advantages, conventional NeRF implementations require camera movement around stationary objects to capture multiple viewpoints, posing logistical challenges in high-throughput phenotyping environments where automated conveyors and rotating pedestals are standard. Multi-camera arrays and LiDAR scanners can provide the necessary viewpoint coverage but remain cost-prohibitive and operationally complex [Medic et al. 2023], while reconstruction quality remains sensitive to lighting variation, occlusion, and motion-induced blur. A stationary-camera NeRF approach would substantially improve scalability and throughput in both phenotyping and postharvest inspection pipelines.

To address these limitations, we introduce **HSI-SC-NeRF**, a stationary-camera hyperspectral multi-channel NeRF reconstruction framework developed for high-throughput agricultural imaging. Rather than moving the camera, the object rotates on a motorized turntable within a custom-built Teflon imaging chamber that provides diffuse, uniform illumination. COLMAP-based pose estimation using ArUco calibration markers, combined with a simulated pose transformation to the camera frame of reference, enables standard NeRF training on the resulting stationary-camera data. A multi-channel NeRF formulation then optimizes reconstruction jointly across all hyperspectral bands via a composite spectral loss and a

two-stage training protocol that separates geometric initialization from radiometric refinement.

The main contributions of this work are:

- (1) A stationary-camera NeRF pipeline with ArUco-based pose estimation and simulated pose transformation, enabling multi-view hyperspectral acquisition without moving the camera.
- (2) A custom Teflon imaging chamber providing diffuse, uniform illumination for consistent and repeatable hyperspectral data acquisition.
- (3) A multi-channel NeRF formulation with a composite spectral loss and two-stage training protocol that jointly optimizes geometry and spectral fidelity across all hyperspectral bands.
- (4) Quantitative validation of spatial reconstruction accuracy and wavelength-resolved spectral fidelity on three agriculturally relevant produce samples.

Taken together, these contributions demonstrate the feasibility of integrating hyperspectral imaging and 3D reconstruction into automated phenotyping and postharvest quality control workflows. The framework is particularly well-suited to high-value crops, and the multi-channel NeRF formulation is of independent interest to the graphics community as a method for capturing physically meaningful spectral data [Boss et al. 2021; Li et al. 2024].

2 Related Work

Hyperspectral Imaging in Agriculture and 3D Reconstruction. Hyperspectral imaging (HSI) has significantly advanced agricultural applications over the past two decades by enabling non-destructive assessment of plant and produce quality [Gowen et al. 2007]. Capturing hundreds of narrow spectral bands spanning the visible to near-infrared spectrum (400–1000 nm), HSI reveals biochemical indicators such as chlorophyll content, water status, and ripeness [Mahlein et al. 2013]. Early approaches integrated HSI with 3D structural data using Structure-from-Motion (SfM), Multi-View Stereo (MVS), LiDAR, or structured light scanners [Paulus et al. 2014]. Although these methods provide accurate spectral and geometric reconstruction, their practical application is constrained by complex hardware, calibration difficulties, and low throughput. Gantry- and turntable-mounted setups have sought to simplify multi-view acquisition, but remain cumbersome due to self-occlusion, inconsistent viewpoint synchronization, and complex data fusion. These limitations underscore the need for scalable techniques capable of simultaneously capturing rich spectral and geometric data in high-throughput agricultural settings.

Neural Radiance Fields for Spectral 3D Reconstruction. Neural Radiance Fields (NeRF) have substantially advanced 3D reconstruction by modeling scenes as continuous volumetric functions learned from multi-view images [Mildenhall et al. 2021]. NeRF approaches have recently been extended beyond RGB to include hyperspectral data, with studies demonstrating robust spectral radiance field learning from limited viewpoints [Chen et al. 2024]. Spec-NeRF, for example, reconstructs spectral radiance fields from RGB cameras with interchangeable filters, reducing hardware complexity [Li et al.

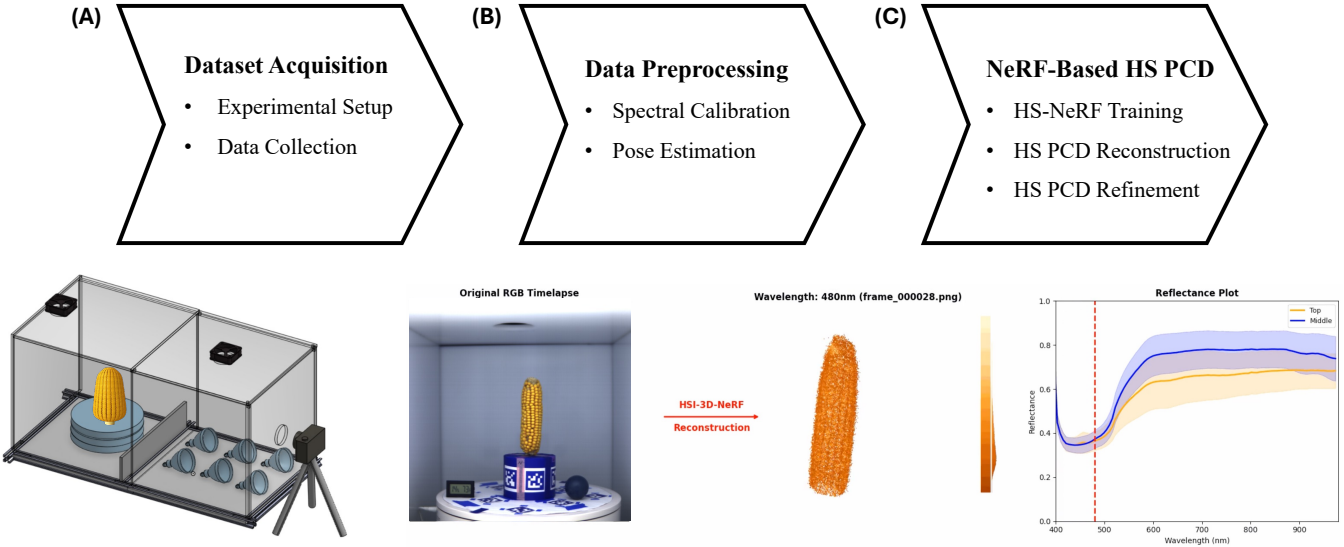


Fig. 3. Workflow of the HSI-SC-NeRF pipeline. The process consists of three main steps: (A) Dataset Acquisition, where the experimental environment is set up and multi-view hyperspectral image data is collected using a stationary camera; (B) Data Preprocessing, involving white-reference spectral calibration and COLMAP-based pose estimation to ensure radiometric and geometric consistency; and (C) NeRF-Based HS PCD, where a multi-channel NeRF model is trained for scene representation, followed by hyperspectral point cloud reconstruction and refinement to generate high-quality 3D hyperspectral point clouds. The graphical abstract (bottom) illustrates the end-to-end pipeline: the imaging chamber with rotating turntable (A), an RGB timelapse frame from the acquisition session (B), the resulting hyperspectral point cloud at 480 nm (C), and per-region reflectance spectra extracted from the reconstructed point cloud (D).

2024]. In agricultural imaging, NeRF-based methods have proven effective for detailed crop reconstruction, accurately estimating traits such as leaf area and fruit volume [Meyer et al. 2024]. Despite these advances, practical limitations persist: the extensive viewpoint coverage required, lengthy capture times, and intensive computational demands continue to hinder deployment in high-throughput contexts.

Limitations of Moving-Camera NeRF in High-Throughput Settings. Traditional NeRF setups require numerous images from varied viewpoints, necessitating camera motion around stationary objects or multi-camera rigs [Gao et al. 2023]. Such setups restrict throughput in agricultural environments due to mechanical complexity, synchronization challenges, and lengthy calibration processes. Maintaining consistent lighting and spectral calibration across multiple viewpoints further exacerbates these issues, leaving moving-camera NeRF implementations predominantly confined to controlled experimental settings and unsuitable for fast-paced industrial or agricultural inspection.

HSI-SC-NeRF. The proposed methodology addresses these limitations through two complementary advances. First, hyperspectral data acquisition is performed with a stationary camera while the object rotates on a motorized turntable within a custom Teflon imaging chamber, simplifying multi-view capture and eliminating the mechanical complexities of traditional setups. Second, the NeRF formulation is extended to predict multi-channel hyperspectral outputs, enabling simultaneous recovery of detailed geometry and spectral reflectance under consistent illumination. Together, these advances

improve scalability and support advanced post-reconstruction analyses such as early disease detection, nutrient assessment, and maturity estimation [Nguyen et al. 2021].

3 Materials and Methods

The HSI-SC-NeRF pipeline, illustrated in Fig. 3, proceeds in three sequential stages. In the **Dataset Acquisition** stage (Section 3.1), an object is rotated on a motorized turntable within a custom Teflon imaging chamber while a stationary SPECIM IQ hyperspectral camera captures one frame every two minutes over a full rotation, yielding 60 frames per object across 204 spectral bands; ArUco markers on the turntable and a 3D-printed cylindrical reference container provide persistent features for pose estimation. In the **Data Preprocessing** stage (Section 3.2), the raw hyperspectral cubes undergo white-reference spectral calibration to correct for wavelength-dependent illumination bias, followed by COLMAP-based pose estimation whose object-frame outputs are transformed to the camera frame of reference via simulated pose transformations. In the final **NeRF-Based Hyperspectral Point Cloud Reconstruction** stage (Section 3.3), a multi-channel NeRF supervised by a composite spectral loss is trained using a two-stage protocol that separates full-frame geometric initialization from masked radiometric fine-tuning, and the trained model is used to reconstruct and refine a dense 3D hyperspectral point cloud.

3.1 Experimental Setup and Data Collection

The experimental setup (Fig. 4) was designed around the SPECIM IQ camera (SPECIM, Spectral Imaging Ltd., Oulu, Finland; <https://www.specim.fi>).

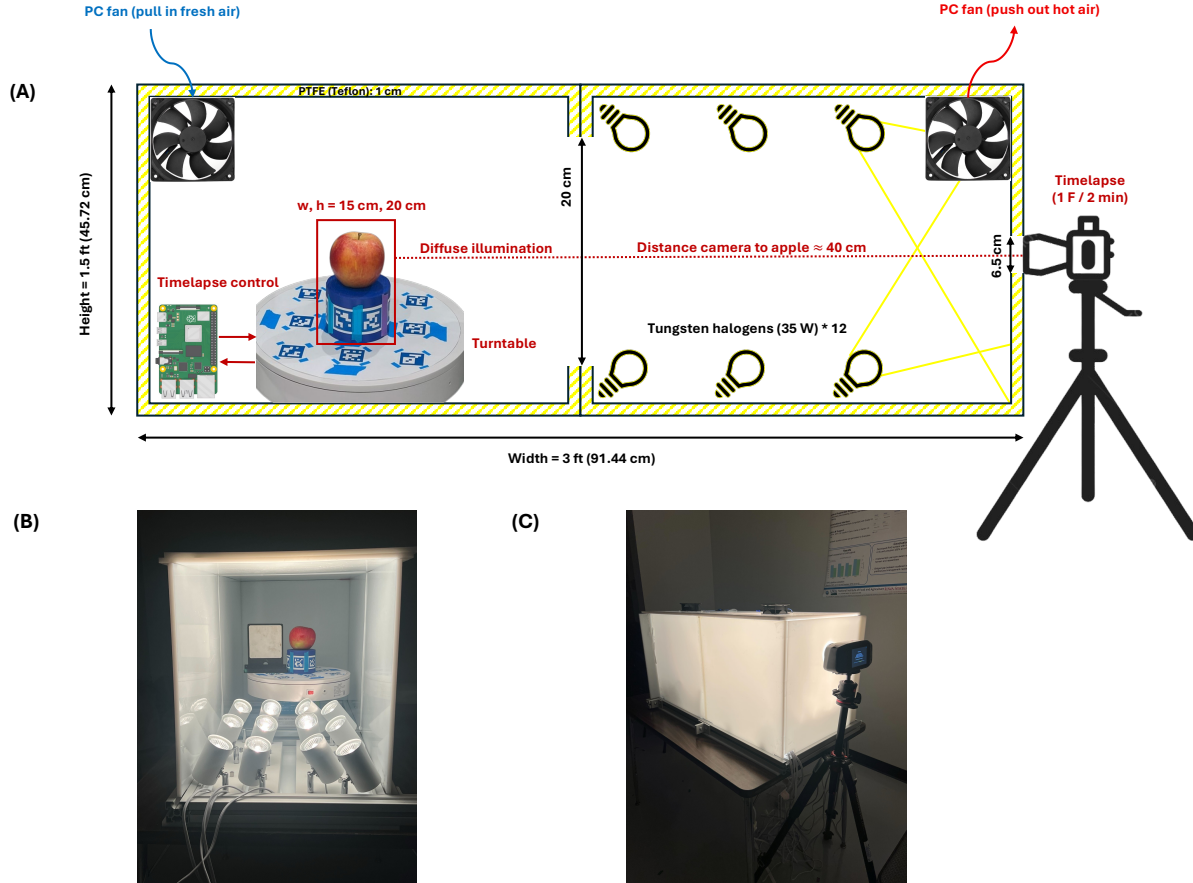


Fig. 4. Teflon studio chamber for uniform hyperspectral illumination. (A) The chamber is designed from PTFE (Teflon) sheets to provide diffuse illumination. (B) Inside the chamber and (C) the outside.

//www.specim.fi/specim-iq/), a portable push-broom hyperspectral imaging system capturing 204 spectral bands from 397 to 1003 nm at a spectral resolution of approximately 7 nm and a spatial resolution of 512×512 pixels in band-interleaved-by-line (BIL) format. The camera was operated with no binning, a frame rate of 100 fps, and an integration time of 10 ms. It was mounted on a tripod, oriented orthogonally to the object, and remained stationary throughout all acquisitions. The object was placed on a motorized rotating turntable inside a custom Teflon (PTFE) imaging chamber lined with twelve 35 W tungsten halogen lamps, whose reflections off the PTFE walls produce the diffuse, spatially uniform illumination required for consistent hyperspectral reflectance measurement. The Teflon background improved foreground segmentation, and the entire setup was placed on a vibration-isolated surface to minimize motion artifacts.

For pose estimation, 5×5 ArUco markers were deployed in two configurations. Six markers were affixed to a custom 3D-printed cylindrical container (diameter 0.09 m, height 0.07 m) designed in OnShape (<https://www.onshape.com/>) and fabricated on an Ultimaker S3 FDM printer. The container's smooth, uniformly colored surface minimized blending artifacts against the Teflon background

and provided a constant radius that maintained continuous marker visibility throughout rotation, addressing geometric inconsistencies common in standard plant pots. Its dimensions were measured with a digital caliper to serve as a metric reference. An additional eight markers were arranged on a circular paper disc mounted to the turntable. Together, these markers provided persistent features for COLMAP to compute camera extrinsic parameters, which is essential in a stationary-camera setup where all parallax and viewpoint variation arises solely from object and marker movement.

The dataset comprised three objects of varying geometry and structural complexity: an apple, a pear, and a maize ear. Each object was positioned individually on the turntable, whose rotation was controlled via a Python script to ensure consistent angular intervals and full surface coverage. A time-lapse acquisition protocol captured one hyperspectral frame every two minutes for a total of 60 frames per object, with each session lasting approximately two hours and yielding 204-band hyperspectral cubes spanning 397.32 to 1003.58 nm. Acquisition speeds can be significantly increased in production settings through faster turntable rotation and reduced inter-frame intervals.

3.2 Data Processing

White Reference-Based Spectral Calibration. To improve spectral consistency under controlled indoor imaging and to mitigate wavelength-dependent illumination and sensor-response bias, we apply a white reference (WR)-based spectral calibration prior to reconstruction (Fig. 5). The complete procedure is provided in Algorithm 1. Let $I(x, y, \lambda)$ denote the captured hyperspectral cube with L spectral bands. The goal is to estimate a stable WR spectrum acquired under identical conditions and use it for band-wise normalization.

WR pixels are first extracted from a coarse region of interest (ROI), Ω_{WR} , selected on a dedicated WR tarp capture. Although the tarp is nominally uniform, spatial non-uniformity typically appears near the boundaries due to illumination falloff and edge effects. To quantify this instability, we compute a per-pixel relative deviation map within Ω_{WR} :

$$D(x, y) = \frac{1}{L} \sum_{\lambda} \left| \frac{I_{\text{WR}}(x, y, \lambda) - \mu_{\text{WR}}(\lambda)}{\mu_{\text{WR}}(\lambda)} \right|, \quad (1)$$

where $I_{\text{WR}}(x, y, \lambda)$ denotes WR pixels and $\mu_{\text{WR}}(\lambda)$ is a preliminary mean WR spectrum computed over the coarse ROI. A refined WR mask is then generated by retaining only pixels satisfying

$$D(x, y) \leq \text{Percentile}_p(D), \quad (2)$$

followed by morphological filtering and largest connected component selection to remove fragmented regions and boundary artifacts. This percentile-based selection yields a spatially contiguous central WR region that preferentially excludes illumination-unstable edge pixels while remaining aligned with the object-centered acquisition geometry (Fig. 5).

The WR mean spectrum is recomputed using only the refined mask Ω_{WR}^* :

$$\mu_{\text{WR}}(\lambda) = \frac{1}{N} \sum_{(x, y) \in \Omega_{\text{WR}}^*} I_{\text{WR}}(x, y, \lambda), \quad (3)$$

where $N = |\Omega_{\text{WR}}^*|$. To suppress residual band-to-band jitter without altering the global spectral trend, $\mu_{\text{WR}}(\lambda)$ is smoothed along the spectral axis using a mild 1-D moving-average operator:

$$\tilde{\mu}_{\text{WR}}(\lambda) = \text{Smooth}[\mu_{\text{WR}}(\lambda)]. \quad (4)$$

Finally, the captured cube is calibrated by band-wise normalization and clipping to the valid reflectance range:

$$I_{\text{cal}}(x, y, \lambda) = \frac{I(x, y, \lambda)}{\tilde{\mu}_{\text{WR}}(\lambda)}, \quad I_{\text{out}}(x, y, \lambda) = \text{clip}(I_{\text{cal}}(x, y, \lambda), 0, 1). \quad (5)$$

As shown in Fig. 5, WR normalization reduces residual illumination bias and improves cross-view consistency in pseudo-RGB renderings, producing reconstructions that more closely match the ground-truth appearance.

Pose Estimation. Feature extraction was performed using COLMAP’s SIFT feature extractor with GPU acceleration. Sequential matching was then applied to establish correspondences between frames, ensuring temporal consistency. Unlike exhaustive matching, which evaluates all possible image pairs, sequential matching assumes an ordered frame sequence, making it well-suited to the smooth, continuous object rotation in our setup while substantially reducing

computational complexity [Feng et al. 2025]. The resulting camera poses estimated for the hyperspectral image sequence are shown in Fig. 6.

The Structure-from-Motion (SfM) pipeline was executed using the COLMAP mapper (v3.12.0), which runs exclusively on the GPU. After evaluating thread counts of 64, 96, and 128, 64 threads were selected as the preferred configuration, as higher counts did not reduce execution time. The sparse point cloud was evaluated based on reprojection error with a target threshold below 1.0 px [Liu et al. 2023], and a bundle adjustment step was applied to jointly refine intrinsic and extrinsic camera parameters.

3.3 NeRF-Based Hyperspectral PCD Reconstruction

We present a neural volumetric reconstruction framework for hyperspectral imaging in which a fixed hyperspectral camera observes a rotating object. This setup ensures consistent illumination across views and reduces calibration complexity, making it well-suited for scanning agricultural produce such as fruits, leaves, and other organic specimens in controlled environments. The multiple hyperspectral channels are used jointly to reconstruct a 3D point cloud of the object.

The method builds directly upon the nerfacto pipeline introduced in NeRFStudio [Tancik et al. 2023], extending it to support hyperspectral inputs by modifying the radiance head to predict an n -dimensional spectral vector and integrating hyperspectral-specific loss terms. Conceptually, the model follows the HS-NeRF architecture proposed in [Chen et al. 2024], specifically the C1, σ_0 variant from their ablation studies, which directly predicts a multi-channel spectral radiance vector while assuming a scalar, wavelength-invariant transmittance, offering improved stability on noisy data. Whereas HS-NeRF generates novel hyperspectral views, the present work extends it to full 3D reconstruction, producing a dense point cloud with per-point hyperspectral channels.

Model Formulation. Let $\mathbf{x} \in \mathbb{R}^3$ denote a point in 3D space and $\mathbf{d} \in \mathbb{S}^2$ the viewing direction. The network predicts an n -channel hyperspectral radiance vector,

$$\mathbf{c}_\lambda = f_c(\Theta_c(\mathbf{x}, \mathbf{d})) \in \mathbb{R}^n, \quad (6)$$

where n is the number of hyperspectral channels, and a scalar transmittance value invariant across wavelength,

$$\bar{\sigma} = f_\sigma(\Theta_\sigma(\mathbf{x})) \in \mathbb{R}. \quad (7)$$

This simplified formulation retains the benefits of a volumetric rendering framework while reducing the cost and instability often associated with learning continuous spectral functions.

Training Protocol. Fig. 7 summarizes the two-stage training procedure. The hyperspectral NeRF is first pre-trained on full-frame inputs to obtain a stable initialization for geometry and coarse spectral alignment, using all pixels in each view so that the model learns a consistent volumetric representation of the scene’s global radiance distribution. The pre-trained checkpoint is then fine-tuned using foreground ROI masks to restrict supervision to object pixels, reducing background-driven gradients and concentrating optimization on radiometrically meaningful regions. Camera optimization is disabled during fine-tuning to decouple radiometric refinement from pose

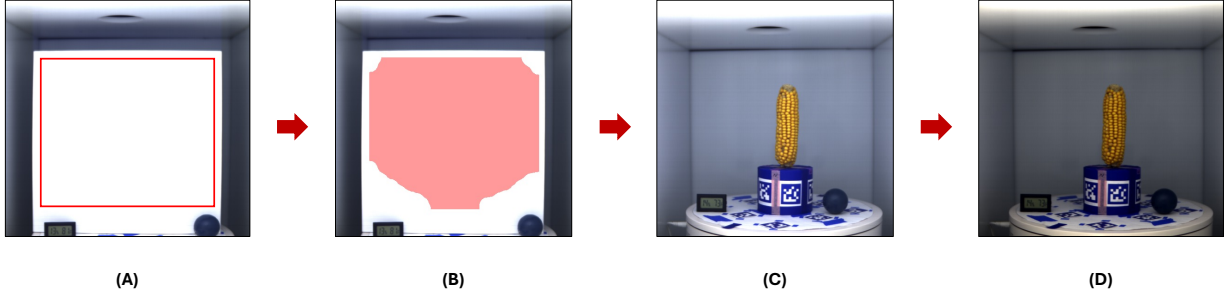


Fig. 5. White reference (WR)-based spectral calibration. (A) Coarse WR region of interest (ROI) extraction. (B) Automatically generated central WR mask after 70th-percentile-based spatial deviation filtering. (C) Pseudo-RGB rendering of the raw hyperspectral cube before calibration. (D) Final spectrally calibrated result after WR-based normalization and reflectance clipping.

Algorithm 1: Spectral calibration using a white reference (WR) tarp with automatic spatial mask generation

1 Input:

- Hyperspectral cube $I(x, y, \lambda)$ with L spectral bands
- Coarse WR region of interest (ROI) Ω_{WR}
- Percentile threshold p for spatial deviation filtering (e.g., $p = 70$)
- 1-D spectral smoothing operator $\text{Smooth}(\cdot)$
- Clipping bounds $[0, 1]$

Output:

- Calibrated hyperspectral cube $I_{\text{out}}(x, y, \lambda)$

Step 1: WR region extraction. Extract WR pixels $I_{\text{WR}}(x, y, \lambda)$ within the coarse ROI Ω_{WR} .

Step 2: Spatial deviation analysis. Compute a per-pixel relative deviation map by averaging over spectral bands:

$$D(x, y) = \frac{1}{L} \sum_{\lambda} \left| \frac{I_{\text{WR}}(x, y, \lambda) - \mu_{\text{WR}}(\lambda)}{\mu_{\text{WR}}(\lambda)} \right|,$$

where $\mu_{\text{WR}}(\lambda)$ is the preliminary mean WR spectrum.

Step 3: Automatic WR mask generation. Generate a refined WR mask by retaining pixels whose deviation satisfies

$$D(x, y) \leq \text{Percentile}_p(D),$$

followed by morphological closing, opening, and largest connected component selection to remove edge-affected regions and illumination falloff artifacts.

Step 4: WR mean spectrum computation. Compute the refined mean WR spectrum over the filtered WR mask:

$$\mu_{\text{WR}}(\lambda) = \frac{1}{N} \sum_{(x, y) \in \Omega_{\text{WR}}^*} I_{\text{WR}}(x, y, \lambda),$$

where $N = |\Omega_{\text{WR}}^*|$.

Step 5: Spectral smoothing. Smooth the mean WR spectrum along the spectral axis:

$$\tilde{\mu}_{\text{WR}}(\lambda) = \text{Smooth}[\mu_{\text{WR}}(\lambda)].$$

Step 6: WR-based normalization. Normalize each pixel spectrum:

$$I_{\text{cal}}(x, y, \lambda) = \frac{I(x, y, \lambda)}{\tilde{\mu}_{\text{WR}}(\lambda)}.$$

Step 7: Final clipping. Clip calibrated intensities to the valid reflectance range:

$$I_{\text{out}}(x, y, \lambda) = \text{clip}(I_{\text{cal}}(x, y, \lambda), 0, 1).$$

return $I_{\text{out}}(x, y, \lambda)$

updates and isolate the effect of hyperspectral supervision. Across both stages, a weighted combination of spectral angular loss and magnitude loss is applied, controlled by $(\lambda_{\text{ang}}, \lambda_{\text{hsd}})$; the final setting is selected via the loss-weight sensitivity analysis in Section 4.4.

Loss Function. The hyperspectral NeRF is trained using a composite objective that combines Nerfacto’s default volumetric rendering

losses from Nerfstudio with hyperspectral-specific spectral supervision:

$$\begin{aligned} \mathcal{L} = & \lambda_{\text{hsd}} \mathcal{L}_{\text{hsd}} + \lambda_{\text{ang}} \mathcal{L}_{\text{ang}} + \lambda_{\text{prop}} \mathcal{L}_{\text{prop}} \\ & + \lambda_{\text{dist}} \mathcal{L}_{\text{dist}} + \lambda_{\text{ori}} \mathcal{L}_{\text{ori}} + \lambda_{\text{pn}} \mathcal{L}_{\text{pn}}. \end{aligned} \quad (8)$$

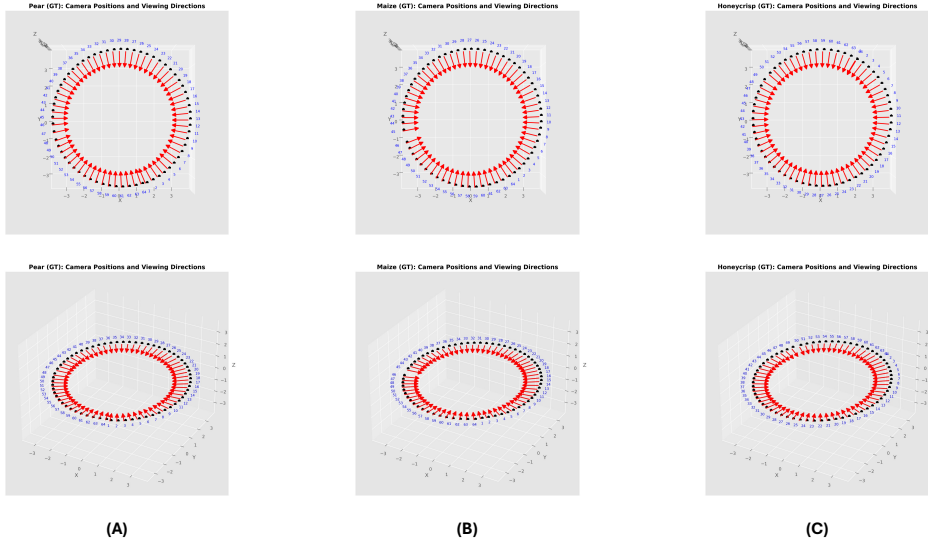


Fig. 6. Camera poses and viewing directions estimated by COLMAP for 64 hyperspectral images. Black squares show camera positions, and red arrows indicate viewing directions toward the object center. (A) Pear, (B) Maize, and (C) Apple.

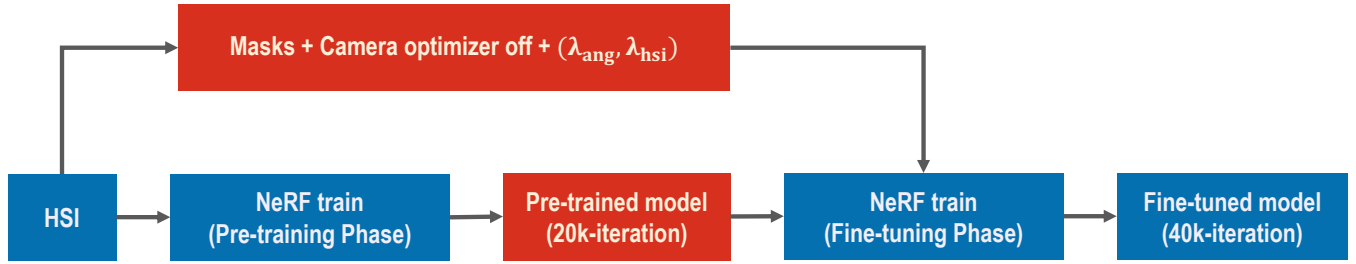


Fig. 7. HSI-SC-NeRF two-stage training protocol. The model is first pre-trained on full-frame HSI, then fine-tuned with foreground masks and the camera optimizer disabled using the selected loss-weight setting $(\lambda_{\text{ang}}, \lambda_{\text{hs}})$. Iteration counts are shown in the diagram.

Hyperspectral Reconstruction Loss (\mathcal{L}_{hs}) is the primary data fidelity term, enforcing accurate recovery of per-pixel spectral radiance across all n wavelength channels via mean squared error over spectral bands:

$$\mathcal{L}_{\text{hs}} = \frac{1}{|\Omega|} \sum_{p \in \Omega} \sum_{i=1}^n \left(\hat{c}_{\lambda_i}^{(p)} - c_{\lambda_i}^{(p)} \right)^2, \quad (9)$$

where p indexes pixels and Ω is the set of valid pixels, optionally selected by a foreground mask.

Angular Spectral Loss (\mathcal{L}_{ang}) encourages agreement in spectral shape independent of overall magnitude by penalizing the angular discrepancy between predicted and ground-truth spectral vectors via cosine similarity. For each valid pixel p , let $\hat{s}(p), s(p) \in \mathbb{R}^{204}$ denote the predicted and target spectra. The cosine similarity is

$$s(p) = \frac{\langle \hat{s}(p), s(p) \rangle}{\| \hat{s}(p) \|_2 \| s(p) \|_2 + \epsilon}, \quad (10)$$

and the loss is defined as

$$\mathcal{L}_{\text{ang}} = \frac{1}{|\Omega|} \sum_{p \in \Omega} (1 - s(p)), \quad (11)$$

where ϵ is a small constant for numerical stability.

Proposal Loss ($\mathcal{L}_{\text{prop}}$), following MipNeRF-360 [Barron et al. 2022], provides coarse-to-fine proposal supervision to stabilize ray sampling and accelerate convergence, which is particularly beneficial for high-channel data where sampling inefficiencies compound during training.

Distortion Regularization ($\mathcal{L}_{\text{dist}}$), following NeRF++ and Instant-NGP [Müller et al. 2022], prevents sample collapse along viewing rays by penalizing excessive contraction of sample intervals, and additionally discourages spectral aliasing due to tightly clustered points.

Orientation Loss (\mathcal{L}_{ori}) encourages surface normals inferred from volumetric gradients to align with known viewing directions,

improving rendering quality and view-consistency on smooth surfaces:

$$\mathcal{L}_{\text{ori}} = \sum_i (1 - \langle \hat{n}_i, v_i \rangle^2), \quad (12)$$

where \hat{n}_i is the predicted normal and v_i is the viewing vector.

Predicted-Normal Loss (\mathcal{L}_{pn}) supervises a normal prediction head by matching predicted normals to computed normals derived from volumetric density gradients, following the Nerfstudio Nerfacto pipeline. For each ray, the predicted normal \hat{n}_j at sample j is compared to the computed normal \hat{n}_j , weighted by the volumetric rendering weight w_j :

$$\mathcal{L}_{\text{pn}} = \mathbb{E}_{\text{rays}} \left[\sum_j w_j \left(1 - \hat{n}_j^\top \hat{n}_j \right) \right], \quad (13)$$

where higher weights correspond to samples that more strongly explain the pixel color. This loss improves surface regularity and view-consistent rendering along high-opacity regions.

In all experiments, Nerfacto's default loss multipliers from Nerfstudio are retained: $\lambda_{\text{prop}}=1.0$, $\lambda_{\text{dist}}=0.002$, $\lambda_{\text{ori}}=10^{-4}$, and $\lambda_{\text{pn}}=10^{-3}$. Only the weights of the two hyperspectral-specific terms, λ_{hs} and λ_{ang} , are tuned, using the cosine variant of \mathcal{L}_{ang} throughout (`angular_loss_type=cosine`).

3.4 Evaluation Metrics

Spatial Evaluation Metrics. The quality of reconstructed point clouds is quantitatively assessed using precision and recall computed after ground-truth alignment [Arshad et al. 2024]. Let \mathcal{P}_{sc} denote the set of stationary-camera NeRF reconstructed points and \mathcal{P}_{gt} the set of ground-truth points obtained from a standard moving-camera NeRF reconstruction. Precision is the fraction of reconstructed points within a threshold distance ϵ of any ground-truth point,

$$\text{Precision}(\epsilon) = \frac{|\{x \in \mathcal{P}_{\text{sc}} \mid \min_{y \in \mathcal{P}_{\text{gt}}} \|x - y\| \leq \epsilon\}|}{|\mathcal{P}_{\text{sc}}|},$$

and recall is the fraction of ground-truth points that have a corresponding reconstructed point within the same threshold,

$$\text{Recall}(\epsilon) = \frac{|\{y \in \mathcal{P}_{\text{gt}} \mid \min_{x \in \mathcal{P}_{\text{sc}}} \|y - x\| \leq \epsilon\}|}{|\mathcal{P}_{\text{gt}}|}.$$

Together, these metrics capture both the inclusion of geometrically relevant surface detail and the exclusion of spurious points.

Spectral Evaluation Metrics. Reconstruction quality on held-out views is evaluated using hyperspectral metrics computed directly on the full spectral cube (204 bands). Let $\hat{s}(p) \in \mathbb{R}^{204}$ and $s(p) \in \mathbb{R}^{204}$ denote the predicted and ground-truth spectral vectors at pixel p , and let Ω be the set of evaluated pixels, optionally restricted by a foreground mask. All metrics are reported as mean \pm standard deviation across held-out views. Spectral fidelity is quantified via spectral RMSE and the spectral angle mapper (SAM), which serve as primary metrics. Hyperspectral PSNR and SSIM are additionally reported as complementary spatial consistency indicators, computed per band and averaged across wavelengths by extending Nerfstudio's default evaluation pipeline to the full 204-band hyperspectral renderings [Tancik et al. 2023].

SAM (Spectral Angle Mapper) [Kruse et al. 1993] measures the angular discrepancy between predicted and ground-truth spectra and is scale-invariant with respect to multiplicative intensity changes:

$$\text{SAM} = \frac{1}{|\Omega|} \sum_{p \in \Omega} \arccos \left(\frac{\langle \hat{s}(p), s(p) \rangle}{\|\hat{s}(p)\|_2 \|s(p)\|_2 + \delta} \right), \quad (14)$$

where δ is a small constant for numerical stability.

Spectral RMSE quantifies cube-level radiometric error. The spectral mean squared error is defined as

$$\text{MSE}_{\text{spectral}} = \frac{1}{|\Omega|} \sum_{p \in \Omega} \frac{1}{204} \| \hat{s}(p) - s(p) \|_2^2, \quad (15)$$

and spectral RMSE is computed as $\text{RMSE}_{\text{spectral}} = \sqrt{\text{MSE}_{\text{spectral}}}$.

HSI-SSIM [Wang et al. 2004] is computed per band and averaged across wavelengths:

$$\text{SSIM}_{\text{HSI}} = \frac{1}{204} \sum_{b=1}^{204} \text{SSIM}(\hat{s}_b, s_b), \quad (16)$$

where the standard single-band SSIM is

$$\text{SSIM}(\hat{s}_b, s_b) = \frac{(2\mu_{\hat{s}_b}\mu_{s_b} + C_1)(2\sigma_{\hat{s}_b s_b} + C_2)}{(\mu_{\hat{s}_b}^2 + \mu_{s_b}^2 + C_1)(\sigma_{\hat{s}_b}^2 + \sigma_{s_b}^2 + C_2)}, \quad (17)$$

with μ , σ^2 , and $\sigma_{\hat{s}_b s_b}$ computed over pixels in Ω , and C_1, C_2 stability constants as in Wang et al. [2004].

HSI-PSNR [Huynh-Thu and Ghanbari 2008] is computed per band from the per-band MSE and averaged across wavelengths:

$$\text{MSE}_b = \frac{1}{|\Omega|} \sum_{p \in \Omega} (\hat{s}_b(p) - s_b(p))^2, \quad (18)$$

$$\text{PSNR}_{\text{HSI}} = \frac{1}{204} \sum_{b=1}^{204} 10 \log_{10} \left(\frac{I_{\text{max}}^2}{\text{MSE}_b + \delta} \right), \quad (19)$$

with $I_{\text{max}} = 1$ after normalization and δ for numerical stability.

4 Results and Discussion

The HSI-SC-NeRF framework is evaluated under criteria relevant to agricultural applications, encompassing spatial reconstruction accuracy, wavelength-resolved spectral fidelity, and sensitivity to loss-weight configuration. The model predicts n -channel radiance vectors with a wavelength-invariant density field, following the C1, σ_0 configuration of Chen et al. [2024], prioritizing robustness, computational efficiency, and noise tolerance for practical deployment.

4.1 Example Applications

The reconstructed 3D hyperspectral point clouds are used to support spatially resolved comparisons of spectral signatures and band-specific volumetric comparisons under a consistent processing pipeline (Fig. 3). For each crop, meaningful spectral bands are selected based on prior studies linking specific wavelengths to key biochemical and physical indicators. These bands are not used during training but serve exclusively for post-reconstruction interpretation of reflectance patterns.

- **Apple:** 551 nm (green band, sensitive to chlorophyll and brown pigments in the peel); 708 nm (red-edge, sensitive to pigment, structure, and water status, and commonly selected for fruit maturity and stress assessment); 801 nm (NIR band in the 800–820 nm region recommended for apple bruise and defect detection) [Baek et al. 2019, 2022; Fsian et al. 2025].
- **Maize Kernel:** 490 nm (pigment variation among cultivars); 580 nm (carotenoid content and maturity); 850 nm (dryness and starch accumulation) [Alimohammadi et al. 2022; Thenkabail et al. 2000].
- **Pear:** 550 nm (green band, sensitive to peel color and chlorophyll content); 710 nm (red-edge, linked to pigment changes, maturity, and internal quality); 980 nm (NIR water-related band associated with internal water status, firmness, and bruise or disease detection) [Lee et al. 2014; Cruz et al. 2021].

These post-reconstruction spectral signatures provide biologically relevant cues for interpreting crop condition and quality, enabling targeted, wavelength-aware evaluation of NeRF-generated reconstructions in an agricultural context.

4.2 Spatial Validation

Spatial reconstruction accuracy was evaluated using a precision-recall analysis based on point-to-surface distances between the reconstructed maize ear and the reference model. After rigid alignment via iterative closest point (ICP) registration in CloudCompare, precision and recall were computed as functions of a distance threshold ϵ , defining the maximum allowable deviation for a predicted surface point to be considered a correct correspondence. As shown in Fig. 8, the optimal threshold was identified at $\epsilon = 0.002$ m (2 mm), at which the reconstruction achieved an F-score of 97.31, indicating strong geometric agreement with the reference. This threshold is conservative relative to the typical kernel thickness of maize ear structures (≈ 5 mm). ICP registration converged with a final RMS point-to-point error of 0.001 m over approximately 50,000 sampled points. The reference model was reconstructed using a rotating RGB camera (iPhone 13 Pro, 2532×1170), while the evaluated reconstruction was generated from hyperspectral imagery captured with a stationary SPECIM camera (512×512).

4.3 Spectral Validation

This section evaluates whether the proposed hyperspectral NeRF preserves wavelength-resolved spectral behavior under radiometrically calibrated inputs. All results correspond to the final training configuration $(\lambda_{\text{ang}}, \lambda_{\text{hsr}}) = (0.25, 0.75)$ selected by the ablation study (Section 4.4), with each dataset split into 90% training views and 10% held-out views. All reported metrics are computed directly on the full 204-band hyperspectral renderings and their corresponding held-out ground truth.

Table 1 summarizes quantitative performance on held-out views for all three crops under the loss-weight setting $(\lambda_{\text{ang}}, \lambda_{\text{hsr}}) = (0.25, 0.75)$. Unlike conventional NeRF evaluation reporting PSNR, SSIM, or LPIPS on RGB images, hyperspectral PSNR and SSIM are computed directly over the full 204-band outputs (band-wise then averaged), together with SAM and spectral RMSE, to assess wavelength-resolved fidelity.

SAM remains well below the default ENVI classification threshold of 0.1 rad [Exelis Visual Information Solutions 2014] across all datasets [Kruse et al. 1993], and spectral RMSE remains low, indicating low spectral-shape discrepancy and low absolute per-band error across wavelengths. Hyperspectral PSNR and SSIM are consistent with these spectral results and fall within or near the range commonly reported for high-quality NeRF reconstructions on standard benchmarks [Mildenhall et al. 2021; Xie et al. 2023], though they are treated as supportive indicators rather than primary criteria, as they can be sensitive to evaluation details and do not fully capture wavelength-resolved fidelity [Tancik et al. 2023]. Note that PSNR/SSIM values computed on 204-band hyperspectral renderings are not directly comparable to RGB-only benchmark reports.

The metrics exhibit a consistent dataset difficulty ordering of Maize → Pear → Apple across all evaluation criteria. This trend is attributable to crop-specific differences in geometry and surface appearance, including shape complexity, texture, and wavelength-dependent reflectance variation such as localized bruising patterns and stronger view-dependent effects, all of which increase reconstruction ambiguity and reduce spatial and spectral agreement.

Qualitative comparisons in Fig. 9 further support these trends, showing that predicted pseudo-RGB renderings closely match held-out ground-truth images across representative viewpoints, with remaining discrepancies primarily occurring around fine structures and view-dependent highlights.

4.4 Ablation on Loss-Weight Sensitivity

To study how hyperspectral 3D reconstruction responds to supervision balance, a controlled loss-weight ablation was performed on the maize ear dataset over five configurations: $(\lambda_{\text{ang}}, \lambda_{\text{hsr}}) \in \{(0, 1), (0.25, 0.75), (0.5, 0.5), (0.75, 0.25), (1, 0)\}$. As shown in Fig. 7, all models were first pre-trained on full frames for 20k iterations to obtain a stable initialization for geometry and coarse spectral alignment, then fine-tuned for an additional 20k iterations using foreground masks to concentrate gradients on object pixels. Camera optimization was disabled during fine-tuning to decouple radiometric refinement from pose updates, enabling a cleaner interpretation of how loss-weighting affects hyperspectral fidelity.

Evaluation Metric Categorization: Spectral Fidelity vs. Spatial Proxies. Both pre-trained and fine-tuned models are evaluated using four metrics: SAM, spectral RMSE, SSIM, and PSNR (Table 2), grouped by their physical relevance to hyperspectral analysis. SAM and spectral RMSE are treated as primary metrics, as they directly quantify wavelength-resolved agreement in spectral shape and magnitude respectively. SSIM and PSNR are reported as secondary spatial proxies. Although standard in NeRF evaluation, PSNR and SSIM do not inherently guarantee wavelength-resolved spectral fidelity: because NeRF-style volume rendering integrates transmittance-weighted radiance samples along a ray [Mildenhall et al. 2021] and is commonly optimized with L2-type objectives, it can favor solutions that minimize average pixel-wise error without corresponding gains in spectral correctness [Amir and Weiss 2021]. SAM and spectral RMSE are therefore emphasized as the primary criteria throughout.

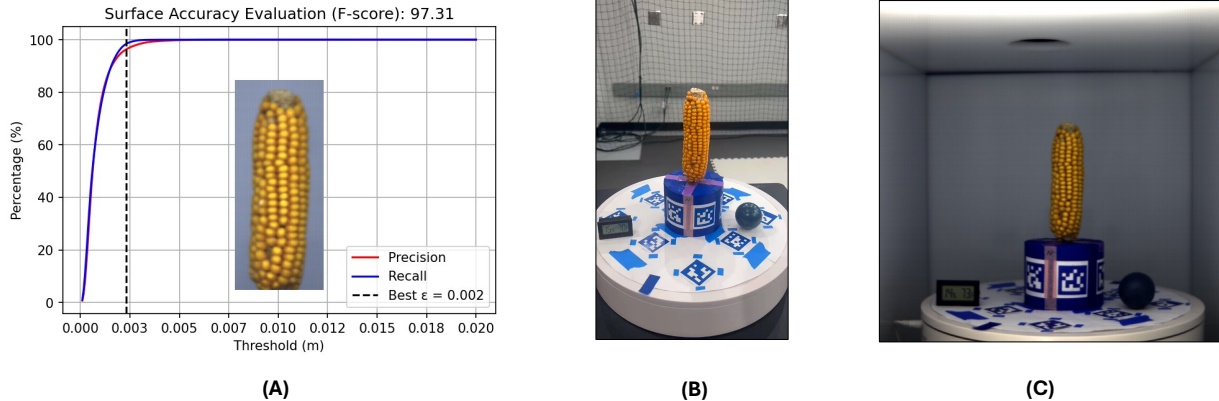


Fig. 8. Spatial validation of maize ear reconstruction. (A) Precision–recall curves as functions of the distance threshold ϵ , with the optimal threshold ($\epsilon = 0.002$ m) indicated by the black dashed line, yielding an F-score of 97.31. Point-to-surface distances were computed after ICP registration in CloudCompare, resulting in a final RMS error of 0.001 m over approximately 50,000 points. (B) Reference PCD obtained using a rotating RGB camera (iPhone 13 Pro, 2532 \times 1170). (C) Predicted PCD generated from hyperspectral imagery captured inside the Teflon imaging chamber using a stationary SPECIM camera (512 \times 512).

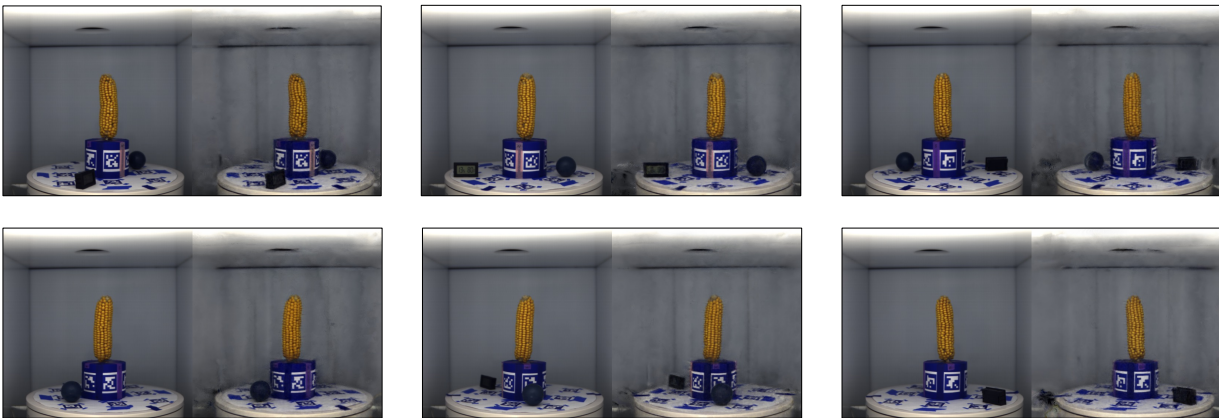


Fig. 9. Evaluation images. Six representative frames (10% of the 64 total frames) are shown. In each maize ear, the left image shows the ground-truth reference and the right image shows the prediction.

Table 1. HSI evaluation metrics with the loss-weight setting $(\lambda_{\text{ang}}, \lambda_{\text{hs}}) = (0.25, 0.75)$ on the 204-band hyperspectral datasets. SAM, RMSE, PSNR, and SSIM are computed directly over the full 204-band hyperspectral renderings. Values are reported as mean \pm SD over held-out views.

| HSI Eval Metrics | Maize | Pear | Apple |
|---------------------------|------------------------|------------------------|------------------------|
| SAM [rad] \downarrow | 0.02921 ± 0.00457 | 0.04577 ± 0.01281 | 0.06420 ± 0.03807 |
| RMSE \downarrow | 0.03051 ± 0.01141 | 0.03242 ± 0.00754 | 0.04383 ± 0.02415 |
| SSIM \uparrow | 0.88823 ± 0.05618 | 0.83259 ± 0.03064 | 0.74229 ± 0.11584 |
| PSNR [dB] \uparrow | 29.13709 ± 2.55173 | 27.47112 ± 3.20361 | 24.49213 ± 5.85267 |
| Number of evaluation rays | 262,144 | | |

Pre-training Phase. In the full-frame pre-training regime, the angular-dominant hybrid (0.75, 0.25) yields the best spectral fidelity, while the balanced setting (0.5, 0.5) performs worst. This ordering

is consistent with the known behavior of SAM: as a measure of angle between spectral vectors, it primarily captures spectral shape agreement and is relatively insensitive to illumination scaling on

Table 2. Pre-trained vs. fine-tuned results on the maize dataset across loss weights ($\lambda_{\text{ang}}, \lambda_{\text{hsd}}$), reported as mean \pm SD over held-out views. Metrics are grouped into spectral fidelity (SAM, RMSE; lower is better) and spatial/image-quality proxies (SSIM, PSNR; higher is better). Best fine-tuned values are highlighted in bold.

| (Angular, HSI) | SAM [0-1] ↓ | | RMSE [0-1] ↓ | | SSIM [0-1] ↑ | | PSNR [dB] ↑ | |
|--------------------|---------------------|---------------------------------------|---------------------|---------------------------------------|---------------------|---------------------------------------|------------------|------------------------------------|
| | Pre-train | Fine-tune | Pre-train | Fine-tune | Pre-train | Fine-tune | Pre-train | Fine-tune |
| (0,1) HSI-only | 0.0622 \pm 0.0113 | 0.0422 \pm 0.0192 | 0.0731 \pm 0.0134 | 0.0360 \pm 0.0141 | 0.3905 \pm 0.1377 | 0.8564 \pm 0.0718 | 22.11 \pm 1.63 | 27.27 \pm 4.43 |
| (0.25,0.75) | 0.0588 \pm 0.0091 | 0.0292 \pm 0.0046 | 0.0715 \pm 0.0098 | 0.0305 \pm 0.0114 | 0.4356 \pm 0.1161 | 0.8882 \pm 0.0562 | 22.17 \pm 1.34 | 29.14 \pm 2.55 |
| (0.5,0.5) | 0.0808 \pm 0.0130 | 0.0523 \pm 0.0204 | 0.0922 \pm 0.0085 | 0.0468 \pm 0.0162 | 0.1758 \pm 0.0972 | 0.7896 \pm 0.0978 | 19.81 \pm 1.11 | 24.45 \pm 3.59 |
| (0.75,0.25) | 0.0498 \pm 0.0087 | 0.0428 \pm 0.0169 | 0.0616 \pm 0.0141 | 0.0421 \pm 0.0138 | 0.5212 \pm 0.1676 | 0.8534 \pm 0.0802 | 23.78 \pm 1.91 | 25.89 \pm 3.94 |
| (1,0) Angular-only | 0.0707 \pm 0.0249 | 0.0381 \pm 0.0162 | 0.0893 \pm 0.0120 | 0.0732 \pm 0.0096 | 0.2811 \pm 0.1276 | 0.5984 \pm 0.0342 | 19.97 \pm 1.51 | 21.65 \pm 1.69 |

calibrated reflectance [Kruse et al. 1993]. Background pixels and view-dependent intensity variation tend to dominate early gradients in full-frame training; emphasizing an angular constraint therefore stabilizes wavelength-wise alignment of the object’s spectral signature, while the magnitude term anchors the intensity scale. Pure angular supervision (1, 0) does not outperform the best hybrid, suggesting that an explicit intensity anchor remains beneficial to limit scale ambiguity during early optimization.

Fine-tuning Phase. After fine-tuning, the optimal configuration shifts to the magnitude-dominant hybrid (0.25, 0.75), exhibiting a clear rank shift relative to pre-training. Once supervision is concentrated on object pixels and pose refinement is disabled, the remaining error becomes primarily radiometric; increasing λ_{hsd} more effectively reduces per-wavelength intensity discrepancies, while retaining a small angular component preserves spectral-shape structure. The angular-only setting (1, 0) shows comparatively strong shape agreement but weaker magnitude accuracy, confirming that scale-invariant objectives alone do not guarantee radiometric correctness. This is consistent with prior work showing that joint pose optimization can absorb photometric error during NeRF training, and that disabling camera optimization in the fine-tuning stage helps isolate radiometric refinement [Lin et al. 2021; Takeda et al. 2023].

Overall, Table 2 confirms that hybrid supervision is more reliable than single-loss baselines, as it jointly constrains spectral shape and magnitude. The optimal weighting is stage-dependent: full-frame pre-training benefits from angular-regularized hybrids, whereas masked fine-tuning with camera optimization disabled favors magnitude-dominant refinement. The configuration (0.25, 0.75) is selected as the final setting for the maize ear dataset, prioritizing wavelength-resolved hyperspectral fidelity.

4.5 Applications: Band-Dependent Visualization and Spectral Separability

To illustrate how hyperspectral reconstructions support application-driven interpretation, a band-dependent visualization analysis was conducted on three produce samples (apple, maize ear, and pear). The central hypothesis is that selecting wavelength triplets targeting biologically and chemically driven reflectance differences can increase spectral separability between tissue states and, in some cases, propagate to downstream geometry-based traits derived from

meshing. For each sample, a baseline pseudo-RGB rendering is compared with an interpretation-driven 3-channel composite; ROI-level spectra are visualized for healthy versus affected regions; and Poisson mesh surface area and volume are reported to assess sensitivity of trait estimates to band selection.

Apple. A standard pseudo-RGB composite is compared with a bruise-oriented triplet designed to emphasize bruise-sensitive wavelength regions. As shown in Fig. 10A–B, the bruise-oriented composite (801, 708, 551 nm) increases contrast of the affected region relative to pseudo-RGB. The ROI spectra (Fig. 10C) indicate consistent reflectance separability between healthy and bruised tissue in the visible range (550–650 nm) and in the red-edge/NIR region (708–801 nm), consistent with wavelength-dependent responses to tissue condition. Poisson surface reconstructions (octree depth 8) generated from each composite show that the bruise-oriented composite yields a smaller surface area and larger volume compared to pseudo-RGB (Table 3), suggesting that band choices altering material-dependent contrast can also affect mesh-derived trait estimates.

Maize. The maize ear is visualized using two 3-channel composites: a visible-band triplet and an NIR-inclusive triplet selected to highlight kernel-level contrast, rendered at [650, 540, 470] nm and [850, 580, 490] nm respectively (Fig. 11A–B). The ROI spectra (Fig. 11C) show localized reflectance variation across anatomical features spanning both the visible and NIR wavelengths. Mesh-derived traits computed from Poisson reconstructions (octree depth 8) are identical across the two composites (Table 3), indicating that while band selection changes visual appearance and spectral contrast, the global mesh geometry remains stable under the current meshing configuration.

Pear. A pseudo-RGB composite is compared with an interpretation-driven triplet selected to emphasize peel-color, red-edge, and water-related responses. The disease-oriented composite (980, 710, 550 nm) increases visibility of quality differences relative to pseudo-RGB (Fig. 12A–B). The ROI spectra (Fig. 12C) show separability between healthy and diseased tissue near 550 nm, 710 nm, and 980 nm, consistent with wavelength-dependent responses to tissue composition and water status. Surface area and volume estimates from Poisson meshes (octree depth 8) remain nearly unchanged across composites (Table 3), suggesting that band selection can

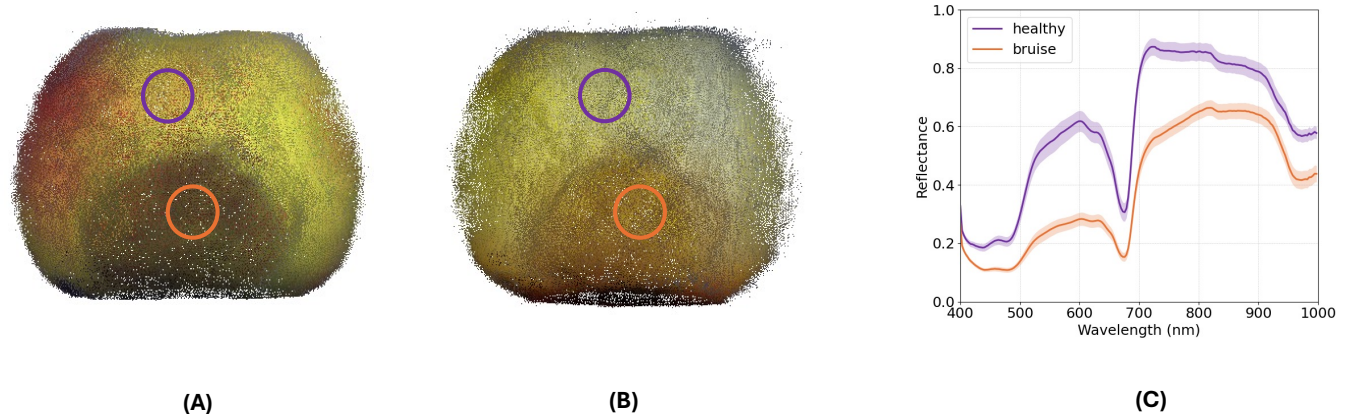


Fig. 10. Apple visualization and spectra. (A) Pseudo-RGB (598, 548, 449 nm). (B) Bruise-contrast composite (801, 708, 551 nm). (C) Mean reflectance spectra from the marked healthy and bruised regions.

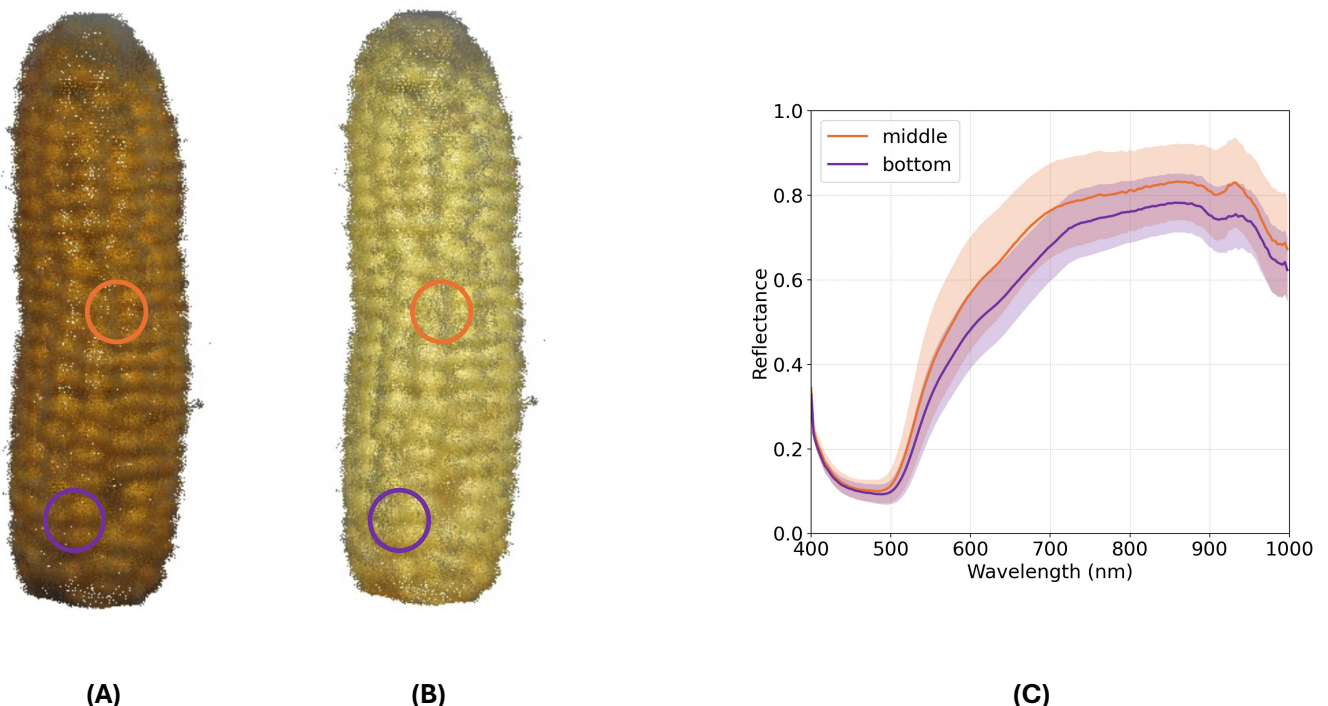


Fig. 11. Maize reconstructions under different band triplets. (A) Visible composite [650, 540, 470] nm. (B) NIR-inclusive maize triplet [850, 580, 490] nm. (C) Spectral reflectance curves extracted from the highlighted surface regions in (A) and (B).

improve spectral separability without perturbing global mesh traits for this sample.

Overall, interpretation-driven band selection enhances spectral separability between biologically distinct tissues and, in some cases, produces measurable differences in mesh-derived geometric traits. The apple case demonstrates that band choices aligned with chemically and structurally driven reflectance changes can propagate

to downstream surface area and volume estimates, whereas the maize and pear examples show comparatively stable global geometry under the same meshing configuration. These results motivate reporting both ROI-level spectra and geometry-based traits when hyperspectral reconstructions are used for phenotyping or postharvest assessment.

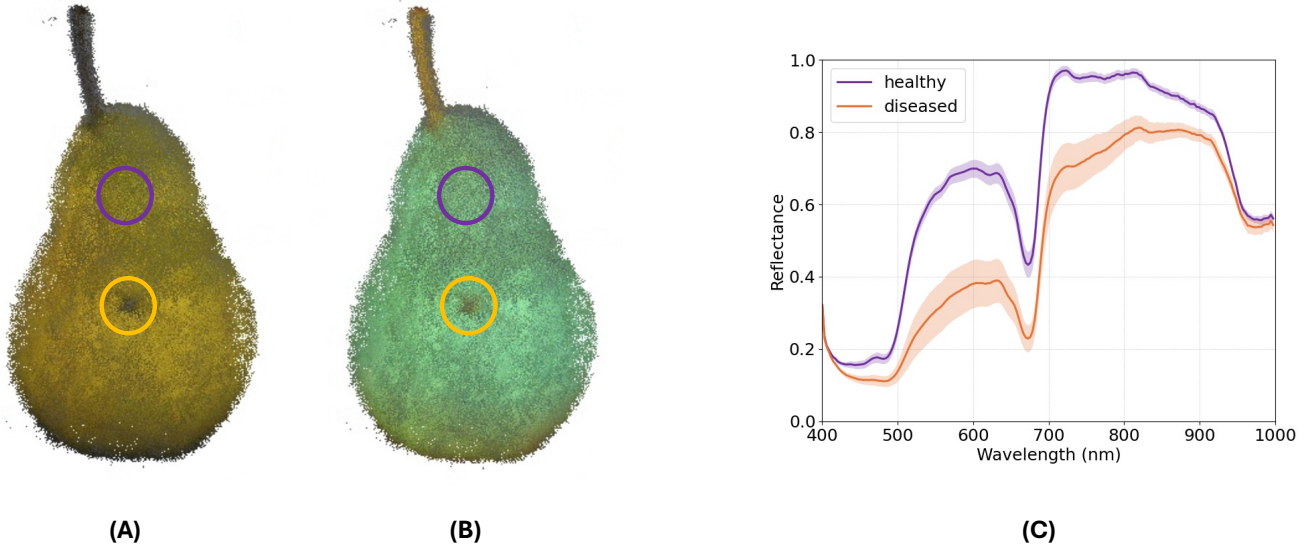


Fig. 12. Pear visualization and spectra. (A) Pseudo-RGB composite. (B) Disease-oriented composite (980, 710, 550 nm). (C) Mean reflectance spectra from the marked healthy and diseased regions.

Table 3. Surface area and volume estimates for Poisson meshes (octree depth 8) reconstructed from different 3-channel composites (Figs. 10–12A–B). Area is reported in m^2 and volume in liters (L).

| Crop | Band composite [nm] | Area (m^2) | Volume (L) |
|-------|-----------------------------------|-----------------------|------------|
| Apple | Pseudo-RGB: [598, 548, 449] | 0.176 | 0.225 |
| | Bruise-contrast: [801, 708, 551] | 0.118 | 0.245 |
| Maize | Visible: [650, 540, 470] | 0.147920 | 0.395930 |
| | NIR-inclusive: [850, 580, 490] | 0.147920 | 0.395930 |
| Pear | Pseudo-RGB | 0.0881612 | 0.125526 |
| | Disease-oriented: [550, 710, 980] | 0.0881611 | 0.125525 |

5 Conclusions

HSI-SC-NeRF is a stationary-camera hyperspectral NeRF framework tailored for agricultural applications requiring joint 3D structural and spectral analysis. Fixed-camera hyperspectral imaging combined with object rotation and simulated pose estimation eliminates the need for complex moving-camera rigs while preserving high-resolution geometry and spectral detail. The framework achieves near-perfect geometric reconstruction (F-score: 97.31%) and captures spectrally meaningful information across the visible and near-infrared spectrum, with the ablation study confirming that a magnitude-dominant hybrid loss with masked fine-tuning yields the best wavelength-resolved fidelity.

Several limitations remain. Spectral accuracy is sensitive to non-uniform illumination, as shadows or lamp drift can introduce reflectance inconsistencies; future work could address this using decomposition techniques such as Nerfactor [Zhang et al. 2021]. The fixed-camera, rotating-object design simplifies hardware but may

limit acquisition speed and requires careful calibration to avoid misalignment. The method also assumes rigid-body motion, which may not hold for soft or deformable objects, and reliance on simulated poses may reduce generalization to more complex or outdoor environments.

The high-fidelity 3D hyperspectral reconstructions produced by HSI-SC-NeRF capture detailed surface geometry and spectral characteristics critical for detecting subtle physiological traits such as early produce damage or stress. For postharvest supply chains, the framework enhances detection of defects including bruising, pathogen infestations, and physiological disorders, reducing waste and improving marketability [Song et al. 2024; Li et al. 2025]. For breeding programs and phenotyping initiatives, it enables non-destructive evaluation of complex traits that combine structural and biochemical components, accelerating selection cycles.

Acknowledgements

This work was supported by the AI Institute for Resilient Agriculture (USDA-NIFA 2021-67021-35329), NSF 2412929/2412928 and Iowa State University's Plant Science Institute.

References

- D. K. Gupta, A. Pagani, P. Zamboni, A. K. Singh, Ai-powered revolution in plant sciences: advancements, applications, and challenges for sustainable agriculture and food security, *Exploration of Foods and Foodomics* 2 (2024) 443–459. doi:[10.37349/eff.2024.00045](https://doi.org/10.37349/eff.2024.00045).
- S. Sarkar, B. Ganapathysubramanian, A. Singh, F. Fotouhi, S. Kar, K. Nagasubramanian, G. Chowdhary, S. Das, G. Kantor, A. Krishnamurthy, N. Merchant, A. Singh, Cyber-agricultural systems for crop breeding and sustainable production, *Trends in Plant Science* 29 (2023). doi:[10.1016/j.tplants.2023.08.001](https://doi.org/10.1016/j.tplants.2023.08.001).
- J.-Y. Song, Z.-S. Qin, C.-W. Xue, L.-F. Bian, C. Yang, Fruit grading system by reconstructed 3d hyperspectral full-surface images, *Postharvest Biology and Technology* 212 (2024) 112898. URL: <https://www.sciencedirect.com/science/article/pii/S0925521424001431>. doi:<https://doi.org/10.1016/j.postharvbio.2024.112898>.

2024.112898.

X. Li, Y. Zhang, L. Chen, J. Wang, H. Liu, Enhanced detection of early bruises in apples using near-infrared hyperspectral imaging with geometrical influence correction for universal size adaptation, *Postharvest Biology and Technology* 211 (2025) 112775. doi:[10.1016/j.postharvbio.2024.112775](https://doi.org/10.1016/j.postharvbio.2024.112775).

A. Eltner, G. Sofia, Structure from motion photogrammetric technique, in: M. J. Westoby, J. Brasington, N. F. Glasser (Eds.), *Developments in Earth Surface Processes*, volume 23, Elsevier, Amsterdam, Netherlands, 2020, pp. 1–24.

R. Chen, S. Han, J. Xu, H. Su, Point-based multi-view stereo network, in: *Proceedings of the IEEE/CVF International Conference on Computer Vision (ICCV)*, IEEE, Seoul, Korea, 2019, pp. 1538–1547.

H. Wang, C. Glennie, Fusion of waveform lidar data and hyperspectral imagery for land cover classification, *ISPRS Journal of Photogrammetry and Remote Sensing* 108 (2015) 1–11. doi:[10.1016/j.isprsjprs.2015.05.012](https://doi.org/10.1016/j.isprsjprs.2015.05.012).

S. Cai, W. Gou, W. Wen, X. Lu, J. Fan, X. Guo, Design and development of a low-cost ugv 3d phenotyping platform with integrated lidar and electric slide rail, *Plants* 12 (2023) 483. URL: <https://www.mdpi.com/2223-7747/12/3/483>. doi:[10.3390/plants12030483](https://doi.org/10.3390/plants12030483).

D. Andújar, M. Calle, C. Fernández-Quintanilla, Á. Ribeiro, J. Dorado, Three-dimensional modeling of weed plants using low-cost photogrammetry, *Sensors* 18 (2018) 1077.

X. Tang, M. Wang, Q. Wang, J. Guo, J. Zhang, Benefits of terrestrial laser scanning for construction qa/qc: a time and cost analysis, *Journal of Management in Engineering* 38 (2022) 1–10.

A. Paturkar, G. Sen Gupta, D. Bailey, Effect on quality of 3d model of plant with change in number and resolution of images used: An investigation, in: *Advances in Signal and Data Processing: Select Proceedings of ICSDP 2019*, volume 703 of *Lecture Notes in Electrical Engineering*, Springer, Singapore, 2021, pp. 377–388. doi:[10.1007/978-981-15-8391-9_28](https://doi.org/10.1007/978-981-15-8391-9_28).

G. Lu, Bird-view 3d reconstruction for crops with repeated textures, in: *Proceedings of the 2023 IEEE/RSJ International Conference on Intelligent Robots and Systems (IROS)*, IEEE, Detroit, MI, USA, 2023, pp. 4263–4270. doi:[10.1109/IROS55552.2023.10341478](https://doi.org/10.1109/IROS55552.2023.10341478).

B. Mildenhall, P. P. Srinivasan, M. Tancik, J. T. Barron, R. Ramamoorthi, R. Ng, Nerf: Representing scenes as neural radiance fields for view synthesis, *Communications of the ACM* 65 (2021) 99–106. doi:[10.1145/3503250](https://doi.org/10.1145/3503250).

H. Cuevas-Velasquez, A.-J. Gallego, R. B. Fisher, Segmentation and 3D reconstruction of rose plants from stereoscopic images, *Computers and electronics in agriculture* 171 (2020) 105296.

J. Feng, M. Saadati, Z. Jubery, A. Jignasu, A. Balu, Y. Li, L. Attigala, P. Schnable, S. Sarkar, B. Ganapathysubramanian, A. Krishnamurthy, 3d reconstruction of plants using probabilistic voxel carving, *Computers and Electronics in Agriculture* 213 (2023) 108248. doi:[10.1016/j.compag.2023.108248](https://doi.org/10.1016/j.compag.2023.108248).

G. Chen, S. K. Narayanan, T. G. Ottou, B. Missaoui, H. Muriki, C. Pradalier, Y. Chen, Hyperspectral neural radiance fields, <https://arxiv.org/abs/2403.14839>, 2024. ArXiv:2403.14839 [cs.CV].

T. Medic, J. Bömer, S. Paulus, Challenges and recommendations for 3d plant phenotyping in agriculture using terrestrial lasers scanners, *ISPRS Annals of the Photogrammetry, Remote Sensing and Spatial Information Sciences* 10 (2023) 1007–1014. doi:[10.5194/isprs-annals-X-1-W1-2023-1007-2023](https://doi.org/10.5194/isprs-annals-X-1-W1-2023-1007-2023).

M. Boss, S. Lombardi, J. Saragih, S. Schönborn, P. Gotardo, M. Zollhöfer, T. Beeler, Nerd: Neural reflectance decomposition from image collections, in: *Proceedings of the IEEE/CVF International Conference on Computer Vision (ICCV)*, IEEE, Montreal, QC, Canada, 2021, pp. 12684–12694.

R. Li, J. Liu, G. Liu, S. Zhang, B. Zeng, S. Liu, Spectralnerf: Physically based spectral rendering with neural radiance field, in: *Proceedings of the AAAI Conference on Artificial Intelligence*, volume 38, 2024, pp. 3154–3162. doi:[10.1609/aaai.v38i4.28099](https://doi.org/10.1609/aaai.v38i4.28099).

A. A. Gowen, C. P. O'Donnell, P. J. Cullen, G. Downey, J. M. Frias, Hyperspectral imaging—an emerging process analytical tool for food quality and safety control, *Trends in food science & technology* 18 (2007) 590–598.

A.-K. Mahlein, T. Rumpf, P. Welke, H.-W. Dehne, L. Plümer, U. Steiner, E.-C. Oerke, Development of spectral indices for detecting and identifying plant diseases, *Remote Sensing of Environment* 128 (2013) 21–30. doi:[10.1016/j.rse.2012.09.019](https://doi.org/10.1016/j.rse.2012.09.019).

S. Paulus, J. Behmann, H. Mahlein, L. Töpfer, Plant 3d laser scanning for precise phenotyping: Measurement of leaf angle, leaf area, and number of leaves, *Sensors* 14 (2014) 4948–4963. doi:[10.3390/s140304948](https://doi.org/10.3390/s140304948).

J. Li, Y. Li, C. Sun, C. Wang, J. Xiang, Spec-nerf: Multi-spectral neural radiance fields, in: *Proceedings of the IEEE International Conference on Acoustics, Speech and Signal Processing (ICASSP)*, IEEE, Seoul, South Korea, 2024, pp. 2485–2489.

L. Meyer, A. Gilson, U. Schmid, M. Stammerer, Fruitnerf: A unified neural radiance field based fruit counting framework, in: *Proceedings of the 2024 IEEE/RSJ International Conference on Intelligent Robots and Systems (IROS)*, IEEE, Abu Dhabi, United Arab Emirates, 2024, pp. 1–8. URL: <https://arxiv.org/abs/2408.06190>. doi:[10.1109/IROS558592.2024.10802065](https://doi.org/10.1109/IROS558592.2024.10802065).

Y. Gao, L. Su, H. Liang, Y. Yue, Y. Yang, M. Fu, Mc-nerf: Multi-camera neural radiance fields for multi-camera image acquisition systems, <https://arxiv.org/abs/2309.07846>, 2023. ArXiv:2309.07846 [cs.CV].

C. Nguyen, V. Sagan, M. Maimaitiyiming, M. Maimaitijiang, S. Bhadra, M. T. Kwasniewski, Early detection of plant viral disease using hyperspectral imaging and deep learning, *Sensors* 21 (2021) 742. doi:[10.3390/s21030742](https://doi.org/10.3390/s21030742).

H. Feng, Z. Zuo, J.-H. Pan, K.-H. Hui, Y.-H. Shao, Q. Dou, W. Xie, Z.-Z. Liu, Wondervise: Extendable 3d scene generation with video generative models, <https://arxiv.org/abs/2503.09160>, 2025. ArXiv:2503.09160 [cs.CV].

S. Liu, W. P. Bonelli, P. Pietrzyk, A. Bucksch, Comparison of open-source three-dimensional reconstruction pipelines for maize-root phenotyping, *The Plant Phenome Journal* 6 (2023) e20068.

M. Tancik, E. Weber, E. Ng, R. Li, B. Yi, T. Wang, A. Kristoffersen, J. Austin, K. Salahi, A. Ahuja, D. Mcallister, J. Kerr, A. Kanazawa, Nerfstudio: A modular framework for neural radiance field development, in: *ACM SIGGRAPH 2023 Conference Proceedings*, Association for Computing Machinery, New York, NY, USA, 2023, pp. 1–12. URL: <https://doi.org/10.1145/3588432.3591516>.

J. T. Barron, B. Mildenhall, D. Verbin, P. P. Srinivasan, P. Hedman, Mip-nerf 360: Unbounded anti-aliased neural radiance fields, in: *Proceedings of the IEEE/CVF Conference on Computer Vision and Pattern Recognition*, IEEE, New Orleans, LA, USA, 2022, pp. 5470–5479.

T. Müller, A. Evans, C. Schied, A. Keller, Instant neural graphics primitives with a multiresolution hash encoding, *ACM Transactions on Graphics (ToG)* 41 (2022) 1–15. doi:[10.1145/3528223.3530127](https://doi.org/10.1145/3528223.3530127).

M. A. Arshad, T. Jubery, J. Aftul, A. Jignasu, A. Balu, B. Ganapathysubramanian, S. Sarkar, A. Krishnamurthy, Evaluating neural radiance fields for 3d plant geometry reconstruction in field conditions, *Plant Phenomics* 6 (2024) 0235. doi:[10.34133/plantphenomics.0235](https://doi.org/10.34133/plantphenomics.0235).

F. A. Kruse, A. B. Lefkoff, J. W. Boardman, K. B. Heidebrecht, A. Shapiro, P. Barloon, A. F. Goetz, The spectral image processing system (sips)—interactive visualization and analysis of imaging spectrometer data, *Remote sensing of environment* 44 (1993) 145–163. doi:[10.1016/0034-4257\(93\)90013-N](https://doi.org/10.1016/0034-4257(93)90013-N).

Z. Wang, A. C. Bovik, H. R. Sheikh, E. P. Simoncelli, Image quality assessment: from error visibility to structural similarity, *IEEE transactions on image processing* 13 (2004) 600–612. doi:[10.1109/TIP.2003.819861](https://doi.org/10.1109/TIP.2003.819861).

Q. Huynh-Thu, M. Ghanbari, Scope of validity of psnr in image/video quality assessment, *Electronics letters* 44 (2008) 800–801. doi:[10.1049/el:20080522](https://doi.org/10.1049/el:20080522).

I. Baek, C. Eggleton, S. Gadsden, M. Kim, Selection of optimal bands for developing multispectral system for inspecting apples for defects, in: *Sensing for Agriculture and Food Quality and Safety XI*, volume 11016, SPIE, 2019, pp. 59–65. doi:[10.1117/12.2520469](https://doi.org/10.1117/12.2520469).

I. Baek, C. Mo, C. Eggleton, S. A. Gadsden, B.-K. Cho, J. Qin, D. E. Chan, M. S. Kim, Determination of spectral resolutions for multispectral detection of apple bruises using visible/near-infrared hyperspectral reflectance imaging, *Frontiers in plant science* 13 (2022) 963591. doi:[10.3389/fpls.2022.963591](https://doi.org/10.3389/fpls.2022.963591).

A. Fsiain, M. A. Khawaja, M. Kresovic, L. Righetto, J. Y. Hardeberg, Apple bruise detection using hyperspectral imaging, in: *Seventeenth International Conference on Digital Image Processing (ICDIP 2025)*, volume 13709, SPIE, 2025, pp. 784–795. doi:[10.1117/12.3075704](https://doi.org/10.1117/12.3075704).

F. Alimohammadi, M. Rasekh, A. H. Afkari Sayyah, Y. Abbaspour-Gilandeh, H. Karami, V. R. Sharabiani, A. Fioravanti, M. Gancarz, P. Findura, D. Kwaśniewski, Hyperspectral imaging coupled with multivariate analysis and artificial intelligence to the classification of maize kernels., *International Agrophysics* 36 (2022) 83–91.

P. S. Thenkabail, R. B. Smith, E. De Pauw, Hyperspectral vegetation indices and their relationships with agricultural crop characteristics, *Remote sensing of Environment* 71 (2000) 158–182.

W.-H. Lee, M. S. Kim, H. Lee, S. R. Delwiche, H. Bae, D.-Y. Kim, B.-K. Cho, Hyperspectral near-infrared imaging for the detection of physical damages of pear, *Journal of Food Engineering* 130 (2014) 1–7. doi:[10.1016/j.jfoodeng.2013.12.032](https://doi.org/10.1016/j.jfoodeng.2013.12.032).

S. Cruz, R. Guerra, A. Brazio, A. M. Cavaco, D. Antunes, D. Passos, Nondestructive simultaneous prediction of internal browning disorder and quality attributes in 'rocha'pear (*pyrus communis* l.) using vis-nir spectroscopy, *Postharvest Biology and Technology* 179 (2021) 111562. doi:[10.1016/j.postharvbio.2021.111562](https://doi.org/10.1016/j.postharvbio.2021.111562).

I. Exelis Visual Information Solutions, ENVI Classic Tutorial: Spectral Angle Mapper (SAM) and Spectral Information Divergence (SID) Classification, Boulder, CO, USA, 2014. URL: https://www.nvsgespatialsoftware.com/portals/0/pdfs/envi/sam_sid_classification.pdf, eNVI Classic Tutorial.

Z. Xie, X. Yang, Y. Yang, Q. Sun, Y. Jiang, H. Wang, Y. Cai, M. Sun, S3im: Stochastic structural similarity and its unreasonable effectiveness for neural fields, in: *Proceedings of the IEEE/CVF International Conference on Computer Vision*, 2023, pp. 18024–18034. doi:[10.1109/ICCV51070.2023.01652](https://doi.org/10.1109/ICCV51070.2023.01652).

D. Amit, Y. Weiss, Understanding and simplifying perceptual distances, in: *Proceedings of the IEEE/CVF Conference on Computer Vision and Pattern Recognition*, 2021, pp. 12226–12235. doi:[10.1109/CVPR46437.2021.01205](https://doi.org/10.1109/CVPR46437.2021.01205).

C.-H. Lin, W.-C. Ma, A. Torralba, S. Lucey, Barf: Bundle-adjusting neural radiance fields, in: *Proceedings of the IEEE/CVF international conference on computer vision*, 2021, pp. 5741–5751. doi:[10.1109/ICCV48922.2021.00569](https://doi.org/10.1109/ICCV48922.2021.00569).

T. Takeda, S. Yamaguchi, K. Sato, K. Fukazawa, S. Morishima, Efficient 3d reconstruction of nerf using camera pose interpolation and photometric bundle adjustment, in: ACM SIGGRAPH 2023 Posters, 2023, pp. 1–2. doi:[10.1145/3588028.3603691](https://doi.org/10.1145/3588028.3603691).

X. Zhang, P. P. Srinivasan, B. Deng, P. Debevec, W. T. Freeman, J. T. Barron, Nerfactor: Neural factorization of shape and reflectance under an unknown illumination, ACM Transactions on Graphics (ToG) 40 (2021) 1–18.

A Automatic central mask generation

To ensure robust spectral calibration, we performed a spatial deviation analysis on the white reference (WR) tarp to automatically identify a uniform and illumination-stable calibration region. A per-pixel relative deviation map was computed by comparing each WR pixel to the band-wise mean WR spectrum, which revealed increased deviation near the tarp edges due to illumination falloff and boundary effects.

As shown in Fig. 13, applying a 70th-percentile threshold yields a spatially contiguous central WR mask that significantly reduces median, 95th-percentile, and maximum relative deviations compared to the unfiltered WR region, while retaining approximately 1.05×10^5 pixels for calibration. Fig. 14 further illustrates the effect of varying the percentile threshold. Lower thresholds (e.g., 65%) are overly restrictive and remove spatially valid WR pixels in the central region, resulting in holes within the mask, whereas higher thresholds (e.g., 75%) begin to include edge-affected and illumination-unstable pixels. The 70th-percentile threshold therefore represents a practical trade-off in which deviation statistics stabilize and spatial coherence in the central region—where the object is located—is preserved. This selection reflects robustness considerations rather than hyperparameter tuning.

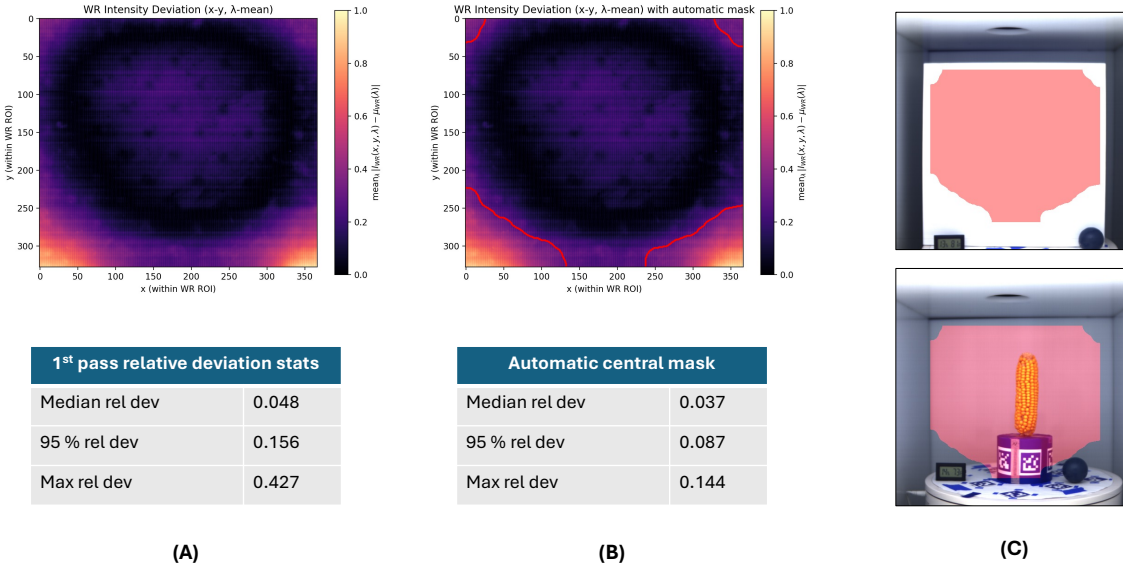


Fig. 13. Automatic central WR mask generated using the 70th-percentile deviation threshold. (A) First-pass spatial relative deviation map computed over the WR region of interest. (B) Refined deviation map and resulting automatic central WR mask after percentile thresholding and morphological filtering. (C) Example acquisition showing the WR tarp and the object positioned at the center of the scene.

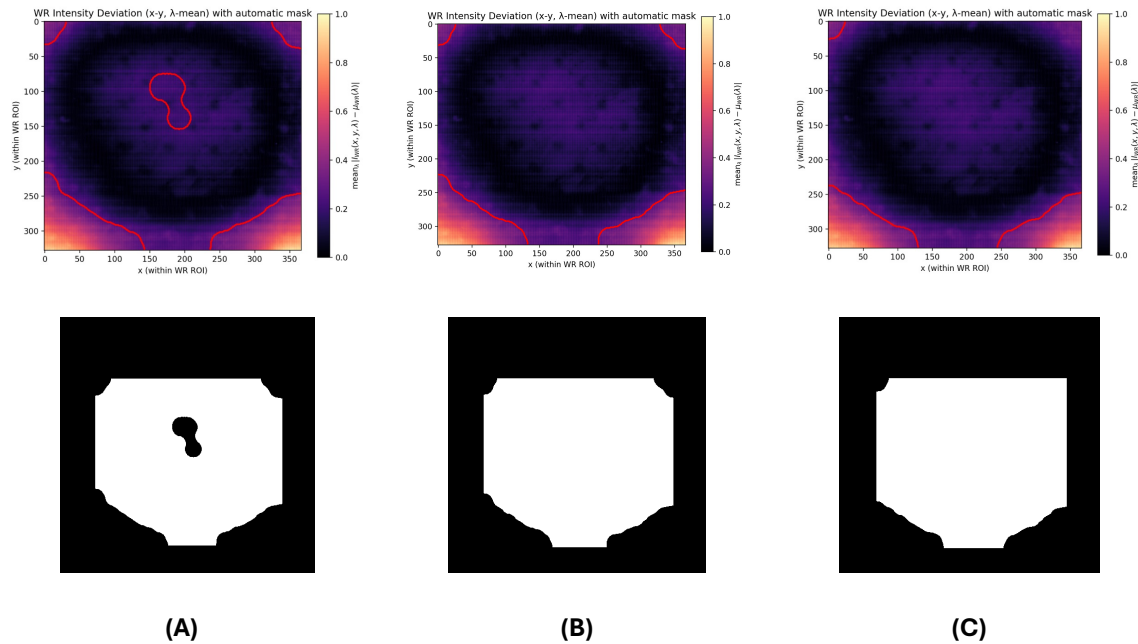


Fig. 14. Justification of the 70th-percentile threshold for automatic WR mask generation. In each pair, the top plot shows the spatial relative deviation map computed within the WR region of interest, and the bottom image shows the corresponding binary WR mask projected onto the original image. (A), (B), and (C) correspond to the 65th-, 70th-, and 75th-percentile thresholds, respectively.